Halimeda tuna (Bryopsidales, Ulvophyceae) calcification on the depth transect in the northern Adriatic Sea; carbonate production on the microscale of individual segments

Yvonne Nemcova[1], Martina Orlando-Bonaca[2] and Jiří Neustupa[1]

[1]Department of Botany, Faculty of Science, Charles University, Prague, Czech Republic
[2]Marine Biology Station Piran, National Institute of Biology, Piran, Slovenia

Corresponding Author:
Yvonne Nemcova[1]
Benatska 2, Praha 2, 12800, Czech Republic
Email address: ynemcova@natur.cuni.cz

Abstract

Halimeda tuna (J. Ellis & Solander) J.V. Lamouroux is the only *Halimeda* species found in the Mediterranean Sea, and it is an important habitat former. In the northern Adriatic, *H. tuna* is among the ten most abundant seaweeds in the upper-infralittoral belt in spring and autumn. The modular thalli consist of serially arranged calcified segments. Calcification is closely related to photosynthesis, which causes alkalinization of the inter-utricular space and triggers aragonite formation. Understanding of the complex patterns of segment shape plasticity in relation to $CaCO_3$ content at different depth levels is still incomplete. Geometric morphometrics was used to investigate *H. tuna* segment shape variation on the depth transect at Cape Madona Nature Monument in the northern Adriatic Sea. The position on the thallus and the $CaCO_3$ content of each studied segment were recorded, allowing slight changes in mineral content to be detected at the microscale of the segments. Our results showed that shape, size, or asymmetry of *H. tuna* segments were not significantly affected by depth. On the other hand, plants that grew deeper were generally more calcified. The apical and subapical segments contributed to the increase in $CaCO_3$ content at the deeper sites, whereas the basal segments did not. This indicates that reniform or oval segments positioned apically or subapically play a key role in calcification of *H. tuna* in Mediterranean ecosystems.

Introduction

The species of the calcifying genus *Halimeda* J. V. Lamouroux (Bryopsidales, Halimedaceae) are important primary producers (*Hillis-Colinvaux, 1980*). They are abundant especially in tropical shallow seas and are major contributors to inter-reef carbonate deposits (*McNeil et al., 2016*). *Halimeda* mud-sustained bioherms along the northern Great Barrier Reef represent

39   important habitats and potential carbon sink; their contribution to the sediment budget may equal
40   or exceed the production of carbonate sediments by stony corals (*McNeil et al., 2016; 2022*). By
41   fixation and long-term storage of atmospheric carbon dioxide in tropical and subtropical reef
42   environments, *Halimeda* provides important ecosystem services (*Mayakun &Prathep, 2019*).
43   Although *Halimeda* spp. are not physical habitat engineers like e.g., calcareous red algae, they
44   effectively contributed to lime muds and sands in the Phanerozoic (*Basso & Granier, 2012;*
45   *Granier, 2012*). *Halimeda tuna* (J. Ellis & Solander) J.V. Lamouroux is the only species thriving
46   in the Mediterranean Sea and is one of the most important biogenic carbonate producers (*Lipej,*
47   *Orlando-Bonaca & Mavrič, 2016*). In the Adriatic Sea, the community dominated by *H. tuna* and
48   the red alga *Mesophyllum alternans* (Foslie) Cabioch & M.L.Mendoza produced about 465 g
49    $CaCO_3$ per m^2 per year (*Canals & Ballesteros, 1997*). Assemblages of *H. tuna* thrive in
50   relatively shallow waters. *Halimeda tuna* may also occur in the Mediterranean Coralligenous
51   formations, a complex of predominantly calcareous-invertebrate biocenoses with important
52   concretion potential, so *Halimeda* fragments may enter the sedimentary record (*Basso et al.*
53   *2022*). In the northern Adriatic, it is also among the ten dominant seaweeds in terms of
54   abundance in spring and autumn samples collected at reference sites for macroalgae in the upper-
55   infralittoral belt (*Orlando-Bonaca & Rotter, 2018*). According to the Ecological Evaluation
56   Index continuous formula (*Orfanidis, Panayotidis & Ugland, 2011*), a multimetric scale-based
57   biotic index that reveals the response of benthic macrophytes to anthropogenic stress, *H. tuna* is
58   included in the first Ecological State Groups (ESG I) with other perennial species, that are
59   indicators of Good/High ecological status of coastal waters (*Orlando-Bonaca, Pitacco & Lipej,*
60   *2021*).
61   *Halimeda* thalli are composed of calcified segments separated by non-calcified nodes. The entire
62   thallus consists of a single branched cell (siphonous thallus). Linear arrays of segments are
63   strung together by medullary siphons that branch to form peripheral utricles (*Hillis-Colinvaux*
64   *1980*). Segments are added consequently, and their production is seasonal, reaching its maximum
65   in summer. However, age of adjacent segments can vary greatly as individual segments and
66   entire segment branches are shed regularly, usually due to physical disturbance and herbivory
67   (*Drew, 1983; Ballesteros 1991*). The peripheral (primary) utricles adhere to each other and form
68   a closed inter-utricular space (IUS) in which aragonite microcrystals precipitate (*Wilbur, Hillis &*
69   *Watabe, 1969, Borowitzka & Larcum, 1977*). The size and shape of peripheral utricles, which
70   have a honeycomb structure when viewed from above, vary among species and represent one of
71   the important identification features (*Borowitzka & Larcum, 1977; Peach et al., 2017*). In
72   addition to among-species differences, variation in size and symmetry of peripheral utricles
73   within a single segment of *H. tuna* has also been demonstrated. The utricles near the segment
74   bases were considerably smaller than those located near the apical and lateral margins, and
75   symmetry of the utricles decreased from the centre to the margins (*Neustupa & Nemcova, 2020*).
76   The inter-utricular space represents a boundary layer that mediates the interaction of algal
77   metabolism with the carbon chemistry of seawater, resulting in $CaCO_3$ precipitation.
78   Calcification is closely linked to photosynthesis, which causes alkalinization of the inter-utricular

79   space and is a trigger for aragonite formation (*Borowitzka & Larcum, 1987; McNicholl, Koch &*
80   *Hofmann, 2019*). However, this process cannot be considered a simple abiotic precipitation
81   because many polysaccharides, proteins, and enzymes are involved (*Wizemann, Meyer &*
82   *Westphal, 2014*). The function of calcification is still matter of debate. It has been suggested that
83   calcification acts as a mechanical support in benthic marine environment, provides carbon
84   dioxide and protons for photosynthesis and nutrient uptake, limits grazing, and prevents attack
85   by parasites and viruses (*Schupp & Paul, 1994; Raven & Giordano, 2009*). The extent of
86   calcification is species-specific; species living in the high-energy regimes usually have smaller
87   and heavily calcified segments (*Multer, 1988; Kooistra & Verbruggeen, 2005*). In general,
88   calcification rate in *Halimeda* spp. is influenced by rate of photosynthesis, light, and nutrient
89   availability (*Vroom et al., 2003; Yniquez, McManus & Collado-Vides, 2010; Pongparadon,*
90   *Nooek & Prathep, 2020*).
91   The shape of the segments can be a relatively plastic feature (*Vroom et al., 2003; Pongparadon,*
92   *Nooek & Prathep, 2020*). *Verbruggen et al. (2005)* evaluated the utility of segment size and
93   shape, assessed by captured by geometric morphometrics and elliptic Fourier analysis, as
94   diagnostic features in *Halimeda* specimens representing the five lineages of the genus delimited
95   by molecular data. Segment size and shape were found to be relatively good predictors of species
96   membership, with the exception of deviated segments (*Verbruggen et al., 2006*). These are
97   apical, non-calcified segments and those from the basal part of the thallus that deviate from the
98   species-typical shape. Plasticity of segment shape in response to environmental factors such as
99   light availability (*Neustupa & Nemcova, 2018; Pongparadon, Nooek & Prathep, 2020*) or wave
100   exposure (*Litter & Litter, 2000; Kooistra & Verbruggen, 2005; Pongparadon, Nooek & Prathep,*
101   *2020*) has also been described.
102   So far, the most detailed description of *H. tuna* segment shape and size plasticity was provided
103   by *Neustupa & Nemcova (2018)*, who studied two populations from the northern Adriatic Sea. A
104   specific developmental pattern of *Halimeda tuna* was revealed. Shape and size of the segment
105   were strongly determined by its position on the thallus. Basally located segments were generally
106   smaller and inversely conical in shape, while segments in the middle and upper part of the thallus
107   were large, oval to reniform in shape. Although both populations were sampled from the same
108   depth in the upper sublittoral, there was a significant difference in the mean shape of the
109   segments, indicating that local environmental factors may have influenced segment
110   morphogenesis (*Neustupa & Nemcova, 2018*). Later, *Neustupa & Nemcova (2022)* examined size
111   and shape plasticity, and calcium carbonate content of *H. tuna* segments in populations along the
112   Adriatic latitudinal gradient. They showed, similarly to the previous study, that segment position
113   on the thallus was the main determinant of its shape. The effect of position outweighed shape
114   differences among plants, populations, and regions. In addition, segment shape proved to be a
115   significant predictor of its $CaCO_3$ content. The reniform and oval segments contained
116   significantly more calcium carbonate than the segments of conversely conical shape.
117   Depth represents a complex environmental variable; habitats on the depth gradient tend to vary
118   in light and nutrient availability, the extent of disturbance, and may undergo varying pressures

119   from herbivores. According to some field observations, thalli of *Halimeda* spp. are more heavily
120   calcified in deeper waters than in shallower ones (*Goreau, 1963*); however, this effect was less
121   pronounced in *H. tuna* (*Böhm, 1973*). On the other hand, calcification rate and $CaCO_3$ content
122   have been described to decrease at low light intensities, which normally correspond to deeper
123   habitats (*Borowitzka & Larkum, 1976; Bandeira-Pedrosa, Pereira & Oliveira, 2004;*
124   *Pongparadon, Nooek & Prathep, 2020)*. Reduced calcification performance observed in *H. tuna*
125   populations under extremely high light irradiance in shallow Florida Keys reef systems was
126   explained by photoinhibition (*Vroom et al. 2003*). *Halimeda* plants growing in shallow, well-
127   irradiated habitats often developed smaller segments than those growing in deeper, shaded
128   localities (*Vroom et al., 2003; Bandeira-Pedrosa, Pereira & Oliveira, 2004; Pongparadon,*
129   *Zuccarello & Prathep, 2017; Pongparadon, Nooek & Prathep, 2020*). Information on depth-
130   dependent segment shape plasticity remains fragmentary (*Pongparadon, Nooek & Prathep,*
131   *2020*). Understanding complex patterns of segment-shape plasticity in relation to $CaCO_3$ content
132   at different depth levels may provide an indication of how individual plants/segments contribute
133   to the overall carbonate budget.
134   Here we present a detailed analysis of *H. tuna* segment shape and size variation on the depth
135   transect at Cape Madona Nature Monument (NM) (northern Adriatic Sea) in relation to calcium
136   carbonate content. The percentage of $CaCO_3$ content was determined for each individual
137   segment. A landmark-based geometric morphometric framework was used to analyze shape and
138   size of the segments. We hypothesize that segments increase in size and calcium carbonate
139   content with increasing depth. We also question whether all segments contribute equally to
140   depth-related calcium carbonate content change.
141

142 ## Materials & Methods

143   Sampling
144   The Gulf of Trieste is an epicontinental, shallow, semi-enclosed sea basin in the northernmost
145   part of the Adriatic Sea with an average depth of almost 21 meters. The Gulf expands from Cape
146   Savudrija (Croatia) to Grado (Italy) and includes the entire Slovenian coast. This area has the
147   lowest winter temperatures in the Mediterranean, usually below 10 °C. The prevailing winds
148   blow mainly from the northeast in an offshore direction (*Boicourt et al., 2021*). In the bottom
149   layer, below 10 m depth, water circulation is mostly counter-clockwise, while at the surface, in a
150   layer about 5 m thick, circulation is driven clockwise by the wind (*Stravisi, 1983*). The coastal
151   zone has been affected by various anthropogenic impacts in recent decades, such as construction,
152   intensive fishing, sewage discharges and mariculture (*Orlando-Bonaca et al., 2015*). However,
153   according to the TRIX index (a combination of loads and impact indicators), water quality
154   conditions of Slovenian coastal waters were recently evaluated as Elevated (*Giovanardi et al.,*
155   *2018*).
156   *Halimeda tuna* thalli were sampled on October 13, 2021, along the depth transect at Cape
157   Madona NM, the westernmost part of the Piran peninsula, Slovenia (45˚31'50"; 45˚31'50") by
158   means of scuba-diving and snorkelling. The Cape Madona NM met the selection criteria for

159   macroalgae reference sites in Slovenian coastal waters (*Orlando-Bonaca & Rotter, 2018*). It is
160   located in the Slovenian water body Sl5VT4, where a large part of the coastal belt is still in its
161   natural state (*Orlando-Bonaca, Lipej & Orfanidis, 2008*). A marked decline in the total coverage
162   of canopy-forming algae, especially for *Cystoseira s.l.* spp., was reported for the macroalgal
163   sampling site at Cape Madona NM in the last decade (*Orlando-Bonaca, Pitacco & Lipej, 2021*).
164   At each depth level (0.5, 2.0, 4.0, 4.9, 6.2 and 9.2 m) ten plants were sampled from 2m × 2m
165   quadrats and light intensity at the seafloor was measured by LI-COR Underwater Quantum
166   Sensor Model Number: LI-192 (90.0, 55.0, 31.0, 29.0, 16,3 and 10.3 $\mu mol \cdot m^{-2} \cdot s^{-1}$, respectively)
167   at 10:10 a.m. In the laboratory, thalli were cleaned from the epiphytes, pressed on absorbent
168   paper, and scanned. The segments composing the longest available series within each plant were
169   used for further analyses, occasionally occurring uncalcified apical segments with incomplete
170   morphogenesis were eliminated. Dataset consisted of 379 segments from 60 different plants
171   comprising the same population. The longest available series of segments vary from 3 to 12
172   segments per plant (average 6.3). Segment positions were labelled: A-basal, B-suprabasal, D-
173   apical (in case of three segments) in longer branches (4 and more segments) all other segments
174   were labelled C-subapical (see Fig. 1).
175
176   Mineral content of segments
177   Segments of the longest available series (composing the longest branch), were carefully
178   separated under the dissecting stereomicroscope, dried at 60°C for 45 minutes and weighed using
179   a precise balance XPR6UD5/M Mettler-Toledo GmbH, Switzerland. Individual segments were
180   decalcified in 5% HCl for 10 min until bubbling had ceased (*Vroom et al., 2003*), rinsed in
181   deionized water, dried (60°C for 45 min) and weighed again. The proportional mineral content of
182   each segment was determined as previously described in (*Neustupa & Nemcova, 2022*). *C = 1-*
183   *dcw/drw*, where *drw* is the total dry weight and *dcw* is the dry weight after decalcification.
184
185   Geometric morphometrics
186   The outlines of individual segments were registered by a series of 80 equidistant two-
187   dimensional points located along their margins. In each segment, the single fixed point
188   (landmark) was located at the position of the basal node. Then, the remaining 79 points were
189   placed in equidistant positions along the segment outlines and treated as semilandmarks in
190   subsequent analyses (*Zelditch, Swiderski & Sheets, 2012*). To minimize potential effects of
191   digitization error that could affect the analysis of shape asymmetry in particular, each segment
192   was registered twice in clockwise and counter-clockwise direction. Subsequently, the counter-
193   clockwise registered points were relabeled to match the order of clockwise digitization. The
194   averaged coordinates from both digitizations were then used for subsequent analyses. The
195   landmark and semilandmark coordinates of segment outlines are listed in Table S1. For the
196   analysis of shape variation among segments, their symmetrical halves were averaged to remove
197   the effects of bilateral asymmetry. In this procedure, each segment was reflected along the axis
198   of bilateral symmetry. Then, the points in the reflected copy were relabeled to match their

199 designation in the original configuration. Finally, the coordinates of the original and mirrored
200 copies were averaged to obtain the ideally symmetric configuration of each segment
201 (*Klingenberg, 2015*).
202 Subsequent shape analyses were based on the coordinates yielded by the generalized Procrustes
203 analysis (GPA), which minimizes the sum of squared distances among corresponding landmarks
204 by removing extraneous information of size, location and orientation (*Zelditch, Swiderski &*
205 *Sheets, 2012; Bookstein, 2018*). Furthermore, the GPA included an additional step consisting of
206 iterative sliding of the semilandmarks along the outline tangents so that their final position
207 resulted in the smoothest possible deformation of the actual configuration relative to the mean
208 shape of the dataset under study (*Bookstein, 1997*).
209 Outline points were digitized using the semi-automated *background curves* tool of TpsDig, ver.
210 2.22 (*Rohlf, 2015*). GPA with sliding of semilandmarks was implemented in TpsRelw, ver. 1.65.
211 Configurations of shapes positioned at the margins of the ordination space were illustrated using
212 TpsRelw, ver. 1.65. Similarly, segment shapes typical of the minimum and maximum values of
213 independent factors reconstructed by the multivariate regression models were illustrated by
214 TpsRegr, ver. 1.50 (*Rohlf, 2015*).
215
216 Statistical analyses
217 Multivariate patterns of shape variation were illustrated by principal component analysis (PCA)
218 of coordinates aligned by GPA. Linear correlations between external factors and individual PCs
219 were shown as vectors in the ordination plot. In addition, the significance of these relationships
220 was evaluated by permutation tests on Pearson's *r* and Spearman's non-parametric rank-order
221 correlation coefficients.
222 The effects of various external factors on the shape characteristics of the segments were
223 evaluated by a series of parallel multivariate regression models. These analyses evaluated the
224 amount of shape variation among configurations, expressed by the Procrustes sum of squares
225 (SS), that could be attributed to each factor. The probabilities of the null hypotheses, which
226 assume that there are no relationships between shape variation among segments and external
227 factors, were assessed by comparing these measured Procrustes SS values with the distribution of
228 random SS yielded by 999 permutations of the original data (*Anderson, 2017; Schaefer et al.,*
229 *2006*). The Bonferroni correction for multiple comparisons was used to set the appropriate limit
230 on the significance of individual models (*Perrett & Mundfrom, 2010*).
231 A total of eight external factors were tested. Depth values spanned six levels according to the
232 sampling design. Mineral content was assessed as proportion of $CaCO_3$ in the dry weight of the
233 segments. Centroid size of the segments, which is defined as the square root of the sum of
234 squared distances of each point from the centroid of their respective configurations, was used as
235 a size measure to assess the shape allometry within the dataset. To assess the relationship of
236 centroid size with segment surface area, surface area was determined using the *curve area* tool of
237 TpsDig, ver. 2.22 (*Rohlf, 2015*). Centroid size (Table S2) was closely linearly correlated with the
238 surface area of the segments (Pearson's r = 0.98), so we used only centroid size for further
239 analyses. Bilateral shape asymmetry was quantified by Procrustes distances between the original
240 and mirrored configurations of each segment. Finally, four binary variables were created to

241 identify the different positions of the segments within the thalli. The relationships among these
242 external factors were evaluated by Spearman's non-parametric rank-order correlation analyses.
243 In addition, Spearman's rank-order correlation was also computed for the relationships of depth
244 and mineral content of the segments at each of the four positions within the thalli. Bonferroni-
245 corrected significance of these correlation analyses was assessed by 999 permutations.
246 PCA of the shape data was performed using TpsRelw, ver. 1.65 (*Rohlf, 2015*). The multivariate
247 regression models were implemented using the function *procD.lm* of the package geomorph, ver.
248 4.0.0 (*Baken et al., 2021*) in R, ver. 4.0.5 (*R Core Team 2021*).

249

Results

251 In the PCA ordination plot the shape data of 379 objects (segments) are represented by points
252 within a morphospace spanned by the first two PCs (Fig. 2). Most of the shape variation (77.6%)
253 was spanned by PC1, which illustrated the shape changes between the broadly reniform
254 segments in the negative part of the axis and the inversely conical segments on the opposite side
255 of PC1. The second most important trend was represented by PC2 (8.9% of shape data variation).
256 This axis illustrated differences between segments with a narrow base and those with more
257 concave outlines. Segment shapes typical for the most marginal occupied positions along these
258 two PC axes are outlined. Segment size differences are not shown in the outlines as the shape
259 variables were size standardized prior to analysis. Size is treated as one of the independent
260 factors projected as vectors onto the morphospace (Fig. 2). The prominent effect of the segment
261 position within the thalli (blue vectors) was clearly demonstrated. Positions "A" and "B" (basal
262 and suprabasal segments) were associated with the right part of the morphospace typical of the
263 inversely conical segments, whereas the segments in positions "C" and "D" (subapical and apical
264 segments) were located in the left part, indicating that these positions contained predominantly
265 reniform segments. Size was represented by a very long vector pointing to the left side of the
266 morphospace. Size was also positively correlated with positions "C" and "D" and the percentage
267 of calcium carbonate content in the segments (grey vector). On the other hand, more asymmetric
268 segments were located in the right part of the morphospace, predominantly occupied by the
269 inversely conical segment shapes in positions "A" and "B" (Fig. 2). Thus, the reniform segments
270 located subapically and apically on the thalli (positions "C" and "D") were larger, more calcified,
271 and more symmetrical compared to the inversely conical segments at the base of the thalli
272 (position "A"), which tended to be smaller, less calcified, and more asymmetrical. Interestingly,
273 depth (green vector) was not significantly correlated with either PC1 or PC2 (Table 1).
274 The multivariate regression models largely confirmed the PCA results. Segment size proved be
275 the most important independent factor, explaining nearly 43% of the shape variation (Table 2).
276 While comparatively smaller segments were clearly typical of inversely conical shapes,
277 increasing size was associated with reniform shapes (Fig. 3A). A very similar shape change was
278 also associated with the varying mineral content of the segments. The reniform segments
279 generally had higher $CaCO_3$ content then the conical-shaped ones (Fig. 3B). However, this
280 regression model accounted for only about 10.8% of the total shape variation. The position of the
281 segments on the thalli proved to be significantly related to their shape (Table 2, Figs 3C–F). The

282   strongest relationship was found for segments located at the base of the thalli (position "A"),
283   which are typical of inversely conical narrow shapes (Fig. 3C). This multivariate regression
284   model explained 21.4% of the total shape variation among segments. In contrast, the subapical
285   and apical segments (positions "C" and "D") typically exhibited the reniform shape (Fig. 3E–F).
286   Depth proved to be virtually independent and unrelated to segment shape and accounted only for
287   a negligible 0.3% of the variation (Table 2).
288   Similarly, depth was largely independent of segment size and their shape asymmetry (Fig. 4). On
289   the other hand, a significant positive relationship was found between depth and mineral content
290   with the non-parametric Spearman's $r_s = 0.21$. This means that plants growing in deeper
291   locations (6–9 m) have slightly more calcified segments than those growing closer to the sea
292   surface. This relationship proved to be even more pronounced for subapical and apical segments
293   in positions "C" ($r_s = 0.33$) and "D" ($r_s = 0.47$). Thus, the segments in the apical position showed
294   the strongest correlation. In contrast, the mineral content of the basal segments in positions "A"
295   and "B" was not significantly related to depth, with $r_s = -0.06$ and $r_s = 0.14$, respectively. The
296   basal segments in position "A" had a significantly lower mineral content with $r_s = -0.35$. On the
297   other hand, the subapical segments in position "C" were typical of a comparatively higher
298    $CaCO_3$ content ($r_s = 0.31$). The suprabasal (position "B") and apical segments (position "D")
299   were not significantly related to mineral content (Fig. 4). The relationship between the different
300   positions and centroid size largely confirmed the pattern established by PCA. Positions "A" and
301   "B" were significantly negatively related to segment size, while the opposite relationship was
302   found for segments located in positions "C" and "D" (Fig. 4).
303    $CaCO_3$ content increased significantly with segment size (Figs 4, 5). The percentage increase in
304    $CaCO_3$ content along the regression line was 15–20%. In addition to the generally smaller basal
305   and suprabasal segments (position "A" and "B"), some of the subapical segments (position "C")
306   were also relatively less calcified. In general, the mineral content of the subapical segments
307   proved to be the most plastic in relation to varying size (Fig. 5). However, even the smallest,
308   most basal segments had a significant amount of $CaCO_3$, although the percentage was much
309   lower compared to the large reniform segments (approximately 30% vs. 87% $CaCO_3$ content).
310

Discussion

312   The marine green macroalga *Halimeda* is an important calcifying organism contributing
313   significantly to the calcium carbonate budget of marine ecosystems (*Hillis-Colinvaux, 1980;*
314   *McNeil et al., 2016*). We still have limited information on calcification performance as a function
315   of depth. Several studies aimed to compare the overall thallus morphology, segment size, and
316   general shape, and to assess $CaCO_3$ content of the whole thalli, usually at two geographically
317   close localities of different depths (*Vroom et al., 2003*) or at a larger number of geographically
318   distant sites (*Pongparadon, Nooek & Prathep, 2020*). In our study we provided a detailed
319   analysis of *H. tuna* segment series, harboring plants on a depth transect comprising six depth
320   levels within the same area. Instead of linear measurements, we applied extremely powerful
321   geometric morphometrics to record and statistically evaluate segment size and shape. In addition,

322   we recorded the position on the thallus and $CaCO_3$ content of each examined segment. Thus, we
323   were able to track slight changes in mineral content on the microscale of the segments.
324   Compared to our previous studies (*Neustupa & Nemcova, 2018; 2022*), the *Halimeda* plants
325   studied, consisted of a lower number of segments (3–12; average 6.3), and therefore only four
326   position categories were defined, compared to our previous study that distinguished five
327   positions (*Neustupa & Nemcova, 2022*).
328   *Rindi et al. (2020)* have shown that all specimens collected from widely scattered locations in the
329   Adriatic Sea share a common haplotype, so we may assume that all our plants sampled on the
330   depth gradient at Cape Madona NM are genetically identical. Shape plasticity of segments within
331   individual thalli indicates the extent of the reaction norm; a range of phenotypes developed by a
332   single genotype over an array of environments, i.e., at different depth-levels. However, the depth
333   factor did not contribute significantly to the observed *H. tuna* segments shape and size variation.
334   Segment shape variation spanned by the first two principal components resembled very closely
335   the results of similar analyses on a larger set of segments (982) from two nearby sublittoral
336   populations (*Neustupa & Nemcova, 2018*) and on a smaller set of segments (535) from distant
337   regions on the Adriatic coast (*Neustupa & Nemcova, 2022*). This is a striking example of the
338   deeply conserved pattern of segment shape plasticity in *H. tuna* applied independently of
339   environmental conditions or location (e.g., latitude). The shape dynamics of segments captured
340   by PC1 was correlated to their position within the thallus, size, asymmetry, and calcium
341   carbonate content (Fig. 2). In this study, we confirm that segments located in the basal part of the
342   thallus were usually smaller, more asymmetric, less calcified, and of inversely conical shape. On
343   the other hand, segments located in the upper part of the thallus were often larger, more
344   symmetrical, more calcified, and of oval to reniform shape (summarized in Fig. 4). *Verbruggen,*
345   *De Clerck & Coppejans, (2005)* referred to the basal aberrant and apical non-calcified segments
346   as "deviant" and suggested that they should be excluded from the morphometric analysis of
347   shape used to distinguish *Halimeda* species.
348   By adjusting size, shape, and resource allocation, macroalgae have a distinct response to light
349   quality and quantity, which is usually correlated with depth. In *Halimeda,* the ability to modify
350   morphology may act as an adaptive mechanism to respond to changing environmental conditions
351   (*Yniquez, McManus & Collado-Vides, 2010*). This can be achieved by altering the overall thallus
352   morphology. In *H. tuna*, *H. discoidea*, *H. opuntia,* and *H. macroloba,* shallow, highly irradiated
353   localities were inhabited by compact, denser branching thalli, whereas in deeper sites with low
354   light intensity brittle, lax branching thalli prevailed (*Bandeira-Pedrosa, Pereira & Oliveira,*
355   *2004; El-Manawy & Shafik, 2008; Pongparadon, Zuccarello & Prathep, 2017; Pongparadon,*
356   *Nooek & Prathep, 2020*). Similarly, the thalli of shallow (4–7 m) growing *H. tuna* in Florida
357   Keys reef systems had fewer segments than those that grew deeper (15–22 m; *Vroom et al.,*
358   *2003*).
359   In general, thalli growing in shallow, well-irradiated habitats developed smaller segments than
360   those growing in deeper, shaded localities (*Bandeira-Pedrosa, Pereira & Oliveira, 2004;*
361   *Pongparadon, Zuccarello & Prathep, 2017; Pongparadon, Nooek & Prathep, 2020; Vroom et*

al., 2003). It has been suggested that larger segments help plants increase their thallus height to

363 improve light exposure (*Pongparadon, Nooek & Prathep, 2020*), or that the greater surface area

364 of the segments may accommodate more chloroplasts in the surface utriculi and thus increase

365 photosynthetic efficiency (*Vroom et al., 2003*). In some species, pronounced shape change was

366 observed as a function of depth/light intensity. *Halimeda opuntia* segment shape changed from

367 reniform under highly irradiated conditions to deeply trilobed in the lower thallus and tripartite

368 shape in the upper thallus under shaded conditions (*Pongparadon, Nooek & Prathep, 2020;* see

369 their figure 1c, d and 2c–h). Similarly, the change in *H. macroloba* segment shape was mainly

370 pronounced in the lower part of the thallus and included the change from ribbed reniform to

371 deeply trilobed shape (*Pongparadon, Nooek & Prathep, 2020*). On the other hand, only slight

372 variation in segment shape was observed in *H. monile* (*El-Manawy & Shafik, 2008*). In our study

373 of *H. tuna* at Cape Madona NM in Slovenia, no variation in segment shape and size was

374 observed as a function of depth. This could be due to a species-specific reaction norm, or our

375 depth gradient was too short (0.5–9.2 m). The rocky bottom at Cape Madona NM reaches the

376 depth of 12 m, and we were able to localize the deepest *H. tuna* populations at 9.2 meters.

377 Out of the factors examined within this study, only calcium carbonate content was found to be

378 significantly influenced by depth. In general, the average $CaCO_3$ content of 60.3% agrees with

379 the values obtained by *Neustupa & Nemcova (2022)* who investigated upper sublittoral *H. tuna*

380 populations over four regions on the latitudinal gradient of the Adriatic Sea (61.6%). Within

381 other investigated Mediterranean Sea populations of this species, lower calcium carbonate

382 content (59.7%) was found by *Prát & Hamáčková (1946)* and *Ballesteros (1991)* (45.7%). On

383 the other hand, slightly higher values (68.1%) were also recorded (*Bilgin & Ertan, 2002*). Only a

384 few studies compared the degree of *Halimeda* spp. calcification between shallow and deep

385 localities. However, the deep and shallow sites were often not within the same region, depth was

386 not explicitly reported, and the extent of calcification was just visually assessed, making the

387 comparison with our results difficult. In general, more heavily calcified plants were found at

388 deeper localities, including *H. tuna* populations from Jamaica (*Goreau, 1961; Böhm, 1973*) and

389 Florida (*Vroom et al., 2003*). Conversely, *Bandeira-Pedrosa, Pereira & Oliveira (2004)* visually

390 evaluated the deep *H. tuna* populations as less calcified. The detailed study in Florida Keys reef

391 systems revealed that *H. tuna* $CaCO_3$ content differed not only between deep (15–22 m; 79.0%

392 in 1997 and 82.9% in 2000) and shallow (4–7 m; 75.0% in 1997 and 75.3% in 2000)

393 populations, but also between the sampling years (*Vroom et al., 2003*). Within our investigation,

394 we found the difference in calcium carbonate content between the shallowest and deepest

395 populations to be comparable to the above-mentioned study. However, our depth gradient was

396 much shorter (0.5–9.2 m). As the *H. tuna* plants growing at the deepest locality (9.2 m) had high

397 $CaCO_3$ content, we assume that they were not light-limited. The increased $CaCO_3$ content in the

398 deep plants may further enhance the light harvesting ability by reflecting photons through the

399 segment (*Vroom et al., 2003*). The lower calcium carbonate content of *H. tuna* individuals at the

400 shallowest locations (0.5 m) in this study could be due to the extremely high irradiation during

401 sunny days, which may result in photoinhibition and lower calcification (*Häder et al., 1996;*

402 *Beach et al., 2003; Vroom et al., 2003*). An alternative explanation is inhibition of carbonic
403 anhydrase, an enzyme that catalyzes the interconversion between carbon dioxide and
404 bicarbonate, resulting in a strong reduction in gross photosynthesis at higher light intensities (*De*
405 *Beer & Larkum, 2001*).
406 Depth was well correlated with light intensity in our study. However, other gradients (e.g.,
407 nutrient availability, extent of disturbance, seasonal temperature stratification, and herbivore
408 pressure) should also be considered. The stable summer temperature stratification in the Gulf of
409 Trieste could be broken by a severe bora wind when warm surface water mixes with a larger
410 quantity of cold intermediate and deep water. Such bora events, typical of the winter season, are
411 not uncommon even in summer (*Crise, Querin & Malačič, 2006*), when the growth of new
412 *Halimeda* segments is maximal. As the only major fish grazer on algae, *Sarpa salpa* Linnaeus,
413 does not usually thrive in calcified thalli (*Ballesteros, 2006; Orlando-Bonaca, Pitacco & Lipej,*
414 *2021*), we do not expect grazing pressure on *Halimeda* to be very high. However, sporadic fish
415 bites were observed on the sampled segments, regardless of the depth from which they were
416 taken.
417 Besides the general finding that calcium content increases with depth, we were able to evaluate
418 how individual segments contribute to this relationship. While the apical (in the "D" position)
419 and subapical ("C" position) segments were the main drivers of this relationship, the calcium
420 carbonate content in the segments located basally on the thallus ("A" and "B" positions) did not
421 change significantly with depth. We hypothesize that this is due to the spatial organization of the
422 filaments in the basal segments, which are tightly interwoven rather than bulging into utriculi,
423 leaving less physical space (smaller inter-utricular space) for calcification. However, this
424 hypothesis would need to be tested by careful transmission electron microscopy studies
425

Conclusions

427 In summary, we found that shape, size, or asymmetry of *H. tuna* segments were not significantly
428 affected by depth. On the other hand, plants growing deeper were more calcified. We also
429 detected slight changes in mineral content at the microscale of the segments. We found that
430 apical and subapical segments contributed to the $CaCO_3$ increase of mineral content at the deeper
431 localities, whereas basal segments did not. Congruently with our previous studies, we confirmed
432 that reniform or oval segments positioned apically or subapically play a key role in calcification
433 of *H. tuna* in Mediterranean ecosystems.
434

Acknowledgements

436 We thank the Marine Biology Station Piran (National Institute of Biology, Slovenia) for
437 providing infrastructure and housing for JN and YN during our field work. Special thanks are
438 due to Milijan Šiško for his valuable help during the fieldwork.
439

References

441 **Anderson MJ. 2017.** Permutational multivariate analysis of variance (PERMANOVA). In:
442   Balakrishnan N, Colton T, Everitt B, Piegorsch W, Ruggeri F, Teugels JL, eds. Wiley
443   StatsRef: Statistics Reference Online. Oxford: Wiley, 1–15 DOI:
444   10.1002/9781118445112.stat07841.
445 **Baken EK, Collyer ML, Kaliontzopoulou A, Adams DC. 2021.** geomorph v4.0 and gmShiny:
446   Enhanced analytics and a new graphical interface for a comprehensive morphometric
447   experience. *Methods in Ecology and Evolution* **12**:2355–2363 DOI: 10.1111/2041-
448   210X.13723.
449 **Ballesteros E. 1991.** Seasonality of growth and production of a deep-water population of
450   *Halimeda tuna* (Chlorophyceae, Caulerpales) in the north-western Mediterranean. *Botanica*
451   *Marina* **34**:291–301 DOI: 10.1515/botm.1991.34.4.291.
452 **Ballesteros E. 2006.** Mediterranean coralligenous assemblages: A synthesis of present
453   knowledge. *Oceanography and Marine Biology* **44**:123–195 DOI: 10.1201/9781420006391-
454   7.
455 **Bandeira-Pedrosa ME, Pereira SMB, Oliveira EC. 2004.** Taxonomy and distribution of the
456   green algal genus *Halimeda* (Bryopsidales, Chlorophyta) in Brazil. *Brazilian Journal of*
457   *Botany* **27**(2) DOI: 10.1590/S0100-84042004000200015.
458 **Basso D, Granier B. 2012.** Calcareous algae in changing environments. *Geodiversitas* **34**: 5–11
459   DOI: 10.5252/g2012n1a1.
460 **Basso D, Bracchi VA, Bazzicalupo P, Martini M, Maspero F, Bavestrello G. 2022.** Living
461   coralligenous as geo-historical structure built by coralline algae. *Frontiers in Earth Science*
462   DOI: 10.3389/feart.2022.961632
463 **Bilgin S, Ertan OO. 2002.** Selected chemical constituents and their seasonal variations in
464   *Flabellia petiolata* (Turra) Nizam and *Halimeda tuna* (Ellis & Sol.) J.V.Lamour in the Gulf
465   of Antalya (North-eastern Mediterranean). *Turkish Journal of Botany* **26**:87–90.
466 **Böhm EL. 1973.** Studies on the mineral content of calcareous algae. *Bulletin of Marine Science*
467   **23**:177–190.
468 **Beach K, Walters L, Vroom P, Smith C, Coyer J, Hunter C. 2003.** Variability in the
469   ecophysiology of *Halimeda* spp. (Chlorophyta, Bryopsidales) on Conch Reef, Florida Keys,
470   USA. *Journal of Phycology* **39**:633–643 DOI: 10.1046/j.1529-8817.2003.02147.x.
471 **Boicourt WC, Ličer M, Li M, Vodopivec M, Malačič V. 2021.** Sea state: recent progress in the
472   context of climate change. In: Malone T, Malej A, Faganeli J, eds. Coastal ecosystems in
473   transition: a comparative analysis of the northern Adriatic and Chesapeake Bay. Geophysical
474   monograph series, 1st ed. Hoboken, American Geophysical Union: Wiley, 21–48 DOI:
475   10.1002/9781119543626.ch3.
476 **Bookstein FL. 1997.** Landmark methods for forms without landmarks: morphometrics of group
477   differences in outline shape. *Medical Image Analysis* **1**:225–243 DOI: 10.1016/S1361-
478   8415(97)85012-8.
479 **Bookstein FL. 2018.** *A Course in Morphometrics for Biologists.* Cambridge, Cambridge Univ.
480   Press.

481 **Borowitzka MA, Larkum AWD. 1976.** Calcification in the green alga *Halimeda*. III. The
482   sources of inorganic carbon for photosynthesis and calcification and a model of the
483   mechanism of calcification. *Journal of Experimental Botany* **27**:879–893. DOI:
484   10.1093/jxb/27.5.879.
485 **Borowitzka MA, Larkum AWD. 1977.** Calcification in the green alga *Halimeda*. I. An
486   ultrastructure study of plant development. *Journal of Phycology* **13**:6–16 DOI:
487   10.1111/j.1529-8817.1977.tb02879.x.
488 **Borowitzka MA, Larkum AWD. 1987.** Calcification in algae: mechanisms and the role of
489   metabolism. *Critical Reviews in Plant Sciences* **6**:1–45 DOI: 10.1080/07352688709382246.
490 **Canals M, Ballesteros E. 1997.** Production of carbonate particles by phytobenthic communities
491   on the Mallorca-Menorca shelf, northwestern Mediterranean Sea. *Deep Sea Research II*
492   **44**:611–629 DOI: 10.1016/S0967-0645(96)00095-1
493 **Crise A, Querin S, Malačič V. 2006.** A strong bora event in the Gulf of Trieste: A numerical
494   study of wind driven circulation in stratified conditions with a pre-operational model. *Acta*
495   *Adriatica* **47** (Suppl.):185–206.
496 **De Beer D, Larkum AWD. 2001.** Photosynthesis and calcification in the calcifying alga
497   *Halimeda discoidea* studied with microsensors. *Plant Cell Environment* **24**: 1209–17 DOI:
498   10.1046/j.1365-3040.2001.00772.x.
499 **Drew EA. 1983.** *Halimeda* biomass, growth rates and sediment generation on reefs in the
500   Central Great Barrier Reef Province. *Coral Reefs* **2**:101–110 DOI: 10.1007/BF02395280.
501 **El-Manawy IM, Shafik MA. 2008.** Morphological characterization of *Halimeda* (Lamouroux)
502   from different biotopes on the Red Sea coral reefs on Egypt. *American-Eurasian journal of*
503   *agricultural & environmental sciences* **3**: 532–538.
504 **Giovanardi F, Francé J, Mozetič P, Precali R. (2018).** Development of ecological
505   classification criteria for the Biological Quality Element phytoplankton for Adriatic and
506   Tyrrhenian coastal waters by means of chlorophyll a (2000/60/EC WFD). *Ecological*
507   *Indicators* **93**:316–332 DOI: 10.1016/j.ecolind.2018.05.015.
508 **Goreau TF. 1963.** Calcium carbonate deposition by coralline algae and corals in relation to their
509   roles as reef-builders. *Annals of the New York Academy of Sciences* **109**:127–167 DOI:
510   10.1111/j.1749-6632.1963.tb13465.x.
511 **Granier B. 2012.** The contribution of calcareous green algae to the production of limestones: a
512   review. *Geodiversitas* **34**:35–60 DOI: 10.5252/g2012n1a3.
513 **Häder DP, Porst M, Herrmann H, Schafer J, Santas R. 1996.** Photoinhibition in the
514   Mediterranean green alga *Halimeda tuna* Ellis et Sol measured *in situ*. *Photochemistry and*
515   *Photobiology* **64**:428–434. DOI: 10.1111/j.1751-1097.1996.tb03087.x.
516 **Hillis-Colinvaux L. (1980).** Ecology and Taxonomy of *Halimeda*: Primary Producer of Coral
517   Reefs. London: Academic Press. DOI: 10.1016/S0065-2881(08)60303-X.
518 **Klingenberg CP. 2015.** Analyzing fluctuating asymmetry with geometric morphometrics:
519   concepts, methods, and applications. *Symmetry* **7**:843–934 DOI: 10.3390/sym7020843.

520 **Kooistra WHCF, Verbruggen H. 2005.** Genetic patterns in the calcified tropical seaweeds
521   *Halimeda opuntia*, *H. distorta*, *H. hederacea*, and *H. minima* (Bryopsidales, Chlorophyta)
522   provide insights in species boundaries and interoceanic dispersal. *Journal of Phycology*
523   **41**:177–187 DOI: 10.1111/j.1529-8817.2005.04095.x.
524 **Lipej L, Orlando-Bonaca M, Mavrič B. 2016.** Biogenic Formations in the Slovenian Sea.
525   Piran: National Institute of Biology, Marine Biology Station Piran.
526 **Littler DS, Littler MM. 2000.** Caribbean Reef Plants: An Identification Guide to the Reef
527   Plants of Caribbean, Bahamas, Florida and Gulf of Mexico. Washington DC: Offshore
528   Graphics.
529 **Mayakun J, Prathep, A. 2019.** Calcium carbonate productivity by *Halimeda macroloba* in the
530   tropical intertidal ecosystem: The significant contributor to global carbonate budgets.
531   *Phycological Research* **67**: 94–101 DOI: 10.1111/pre.12361.
532 **McNeil MA, Webster JM, Beaman RJ, Graham TL. 2016.** New constraints on the spatial
533   distribution and morphology of the *Halimeda* bioherms of the Great Barrier Reef,
534   Australia. *Coral Reefs* **35**:1343–1355 DOI: 10.1007/s00338-016-1492-2.
535 **McNeil M, Nothdurft LD, Hua Q, Webster JM, Moss P. 2021.** Evolution of the inter-reef
536   *Halimeda* carbonate factory in response to Holocene sea-level and environmental change in
537   the Great Barrier Reef. *Quaternary Science Reviews* **277**:107347 DOI:
538   10.1016/j.quascirev.2021.107347.
539 **McNicholl C, Koch MS, Hofmann LC. 2019.** Photosynthesis and light-dependent proton
540   pumps increase boundary layer pH in tropical macroalgae: a proposed mechanism to sustain
541   calcification under ocean acidification. *Journal of Experimental Marine Biology and*
542   *Ecology* **521**:151208 DOI: 10.1016/j.jembe.2019.151208.
543 **Multer HG. 1988.** Growth rate, ultrastructure and sediment contribution of *Halimeda incrassata*
544   and *Halimeda monile*, Nonsuch and Falmouth Bays, Antigua, W.I. *Coral Reefs* **6**:179–186
545   DOI: 10.1007/BF00302014.
546 **Neustupa J, Nemcova Y. 2018.** Morphological allometry constrains symmetric shape variation,
547   but not asymmetry, of *Halimeda tuna* (Bryopsidales, Ulvophyceae) segments. *PLoS ONE*
548   **13**:e0206492 DOI: 10.1371/journal.pone.0206492.
549 **Neustupa J, Nemcova Y. 2020.** Morphometric analysis of surface utricles in *Halimeda tuna*
550   (Bryopsidales, Ulvophyceae) reveals variation in their size and symmetry within individual
551   segments. *Symmetry* **12**:1271 DOI: 10.3390/sym12081271.
552 **Neustupa J, Nemcova Y. 2022.** Geometric morphometrics shows a close relationship between
553   the shape features, position on thalli, and $CaCO_3$ content of segments in *Halimeda tuna*
554   (Bryopsidales, Ulvophyceae). *Hydrobiologia* **849**:2581–2594 DOI: 10.1007/s10750-022-
555   04876-y.
556 **Orfanidis S, Panayotidis P, Ugland KI. 2011.** Ecological Evaluation Index continuous formula
557   (EEI-c) application: a step forward for functional groups, the formula and reference
558   condition values. *Mediterranean Marine Science* **12**:199–231 DOI: 10.12681/mms.60.

559 **Orlando-Bonaca M, Lipej L, Orfanidis S. 2008.** Benthic macrophytes as a tool for delineating,
560   monitoring and assessing ecological status: the case of Slovenian coastal waters. *Marine*
561   *Pollution Bulletin* **56**:666–676 DOI: 10.1016/j.marpolbul.2007.12.018.
562 **Orlando-Bonaca M, Francé J, Mavrič B, Grego M, Lipej L, Flander-Putrle V, Šiško M,**
563   **Falace A. 2015.** A new index (MediSkew) for the assessment of the *Cymodocea nodosa*
564   (Ucria) Ascherson meadow's status. *Marine Environmental Research* **110**:132–141 DOI:
565   10.1016/j.marenvres.2015.08.009.
566 **Orlando-Bonaca M, Rotter A. 2018.** Any signs of replacement of canopy-forming algae by
567   turf-forming algae in the northern Adriatic Sea? *Ecological Indicators* **87**:272–284 DOI:
568   10.1016/j.ecolind.2017.12.059.
569 **Orlando-Bonaca M, Pitacco V, Lipej L. 2021.** Loss of canopy-forming algal richness and
570   coverage in the northern Adriatic Sea. *Ecological Indicators* **125**:107501 DOI:
571   10.1016/j.ecolind.2021.107501.
572 **Peach KE, Koch MS, Blackwelder PL, Guerrero-Given D, Kamasawa N. 2017.** Primary
573   utricle structure of six *Halimeda* species and potential relevance for ocean acidification
574   tolerance. *Botanica Marina* **60**:1–11 DOI: 10.1515/bot-2016-0055.
575 **Perrett JJ, Mundfrom DJ. 2010.** Bonferroni procedure. In: Salkind NJ, ed. *Encyclopedia of*
576   *Research Design.* Thousand Oaks: SAGE Publications, 98–101.
577 **Pongparadon S, Zuccarello GC, Prathep A. 2017.** High morpho-anatomical variability in
578   *Halimeda macroloba* (Bryopsidales, Chlorophyta) in Thai waters. *Phycological Research*
579   **65**:136–145 DOI: 10.1111/pre.12172.
580 **Pongparadon S, Nooek S, Prathep A. 2020.** Phenotypic plasticity and morphological
581   adaptation of *Halimeda opuntia* (Bryopsidales, Chlorophyta) to light intensity. *Phycological*
582   *Research* **68**:115–125 DOI: 10.1111/pre.12404.
583 **Prát S., Hamáčková J. 1946.** The analysis of calcareous marine algae. *Studia Botanica*
584   *Čechoslovaca* **7**:112–126.
585 **R Core Team. 2021.** R: A language and environment for statistical computing. R Foundation for
586   Statistical Computing. *Available at https://www.R-project.org.* (accessed 21 October 2022).
587 **Raven JA, Giordano M. 2009.** Biomineralization by photosynthetic organisms: Evidence of
588   coevolution of the organisms and their environment? *Geobiology* **7**:140–154 DOI:
589   10.1111/j.1472-4669.2008.00181.x.
590 **Rindi F, Pasella MM, Lee MFE, Verbruggen H. 2020.** Phylogeography of the mediterranean
591   green seaweed *Halimeda tuna* (Ulvophyceae, Chlorophyta). *Journal of Phycology* **56**:1109–
592   1113 DOI: 10.1111/jpy.13006.
593 **Rohlf FJ. 2015.** The tps series of software. *Hystrix the Italian Journal of Mammalogy* **26**:9–12
594   DOI: 10.4404/hystrix-26.1-11264.
595 **Schaefer K, Lauc T, Mitteroecker P, Gunz P, Bookstein FL. 2006.** Dental arch asymmetry in
596   an isolated Adriatic community. *American Journal of Physical Anthropology* **129**:132–142.
597   DOI: 10.1002/ajpa.20224.

598 **Schupp PJ, Paul VJ. 1994.** Calcium carbonate and secondary metabolites in tropical seaweeds:
599   variable effects on herbivorous fishes. *Ecology* **75**:1172–1185 DOI: 10.2307/1939440.
600 **Stravisi F. 1983.** The vertical structure annual cycle of the mass field parameters in the Gulf of
601   Trieste. *Bollettino di Oceanologica Teorica ed Applicata* **1**:239–250.
602 **Verbruggen H, De Clerck O, Cocquyt E, Kooistra WHCF, Coppejans E. 2005.** A
603   morphometric approach towards taxonomy in siphonous green algae: a methodological
604   study within the genus *Halimeda* (Bryopsidales*). Journal of Phycology* **41**:126–139 DOI:
605   10.1111/j.1529-8817.2005.04080.x.
606 **Verbruggen H, De Clerck O, Coppejans E. 2005.** Deviant segments hamper a morphometric
607   approach towards *Halimeda* taxonomy. *Cryptogamie Algologie* **26**:259–274.
608 **Verbruggen H, De Clerck O, N'yeurt ADR, Spalding H, Vroom PS. 2006.** Phylogeny and
609   taxonomy of *Halimeda incrassata*, including descriptions of *H. kanaloana* and *H.*
610   *heteromorpha* spp. nov. (Bryopsidales, Chlorophyta). *European Journal of Phycology*
611   **41**:337–362 DOI: 10.1080/09670260600709315.
612 **Vroom PS, Smith CM, Coyer JA, Walters LJ, Hunter CL, Beach KS, Smith JE. 2003.** Field
613   biology of *Halimeda tuna* (Bryopsidales, Chlorophyta) across a depth gradient: comparative
614   growth, survivorship, recruitment, and reproduction. *Hydrobiologia* **501**:149–166 DOI:
615   10.1023/A:1026287816324.
616 **Wilbur KM, Hillis L. (as Colinvaux L.), Watabe N. 1969.** Electron microscope study of
617   calcification in the alga *Halimeda* (order Siphonales). *Phycologia* **8**:27–35 DOI:
618   10.2216/i0031-8884-8-1-27.1.
619 **Wizemann A, Meyer FW, Westphal H. 2014.** A new model for the calcification of the green
620   macro-alga *Halimeda opuntia* (Lamouroux). *Coral Reefs* **33**: 951–964 DOI:
621   10.1007/s00338-014-1183-9.
622 **Yniguez AT, McManus JW, Collado-Vides L. 2010.** Capturing the dynamics in benthic
623   structures: environmental effects on morphology in the macroalgal genera *Halimeda* and
624   *Dictyota*. *Marine Ecology Progress Series* **411**:17–32 DOI: 10.3354/meps08643.
625 **Water Framework Directive. 2000.** Directive 2000/60/EC of the European Parliament and of
626   the Council of 23 October 2000 establishing a framework for Community action in the field
627   of water policy. *Available at* [https://www.eea.europa.eu/policy-documents/directive-2000-](https://www.eea.europa.eu/policy-documents/directive-2000-60-ec-of)
628   [60-ec-of](https://www.eea.europa.eu/policy-documents/directive-2000-60-ec-of) (accessed 27 October 2022).
629 **Zelditch ML, Swiderski DL, Sheets DH. 2012.** Geometric morphometrics for biologists: a
630   primer. 2nd ed. London: Academic Press

Figure 1

Halimeda tuna thallus and designation of the segment positions.

(A) *H. tuna* thallus consisting of 7 segments; Bar = 1 cm. (B) Designation of the segment positions on the thallus of *H. tuna*: A-basal (dark blue), B-suprabasal (light blue), C-subapical (ochre), D-apical (yellow). Shapes of *H. tuna* segments: 1- reniform, 2-oval, 3-inversely conical. Note that the segments of irregular shape may also be present.
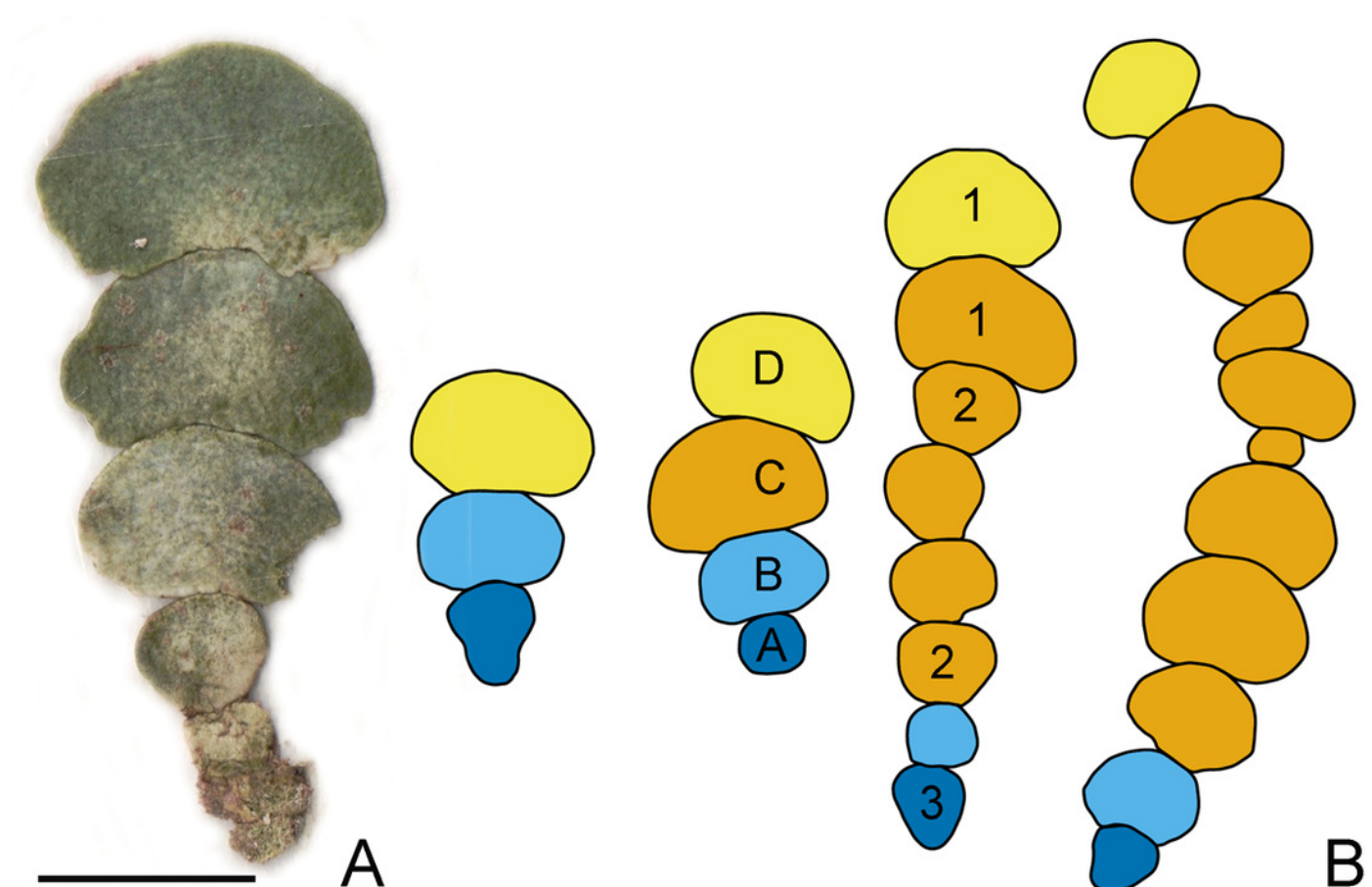
Figure 2

PCA ordination plot of the segment shape data showing first two PCs (PC1 vs. PC2).

The configurations illustrate shapes typical for the most marginal occupied positions on each PC. Independent factors (depth, size, calcium carbonate content, asymmetry, and the positions of the segment along the branch A, B, C and D) are projected as vectors onto the morphospace.
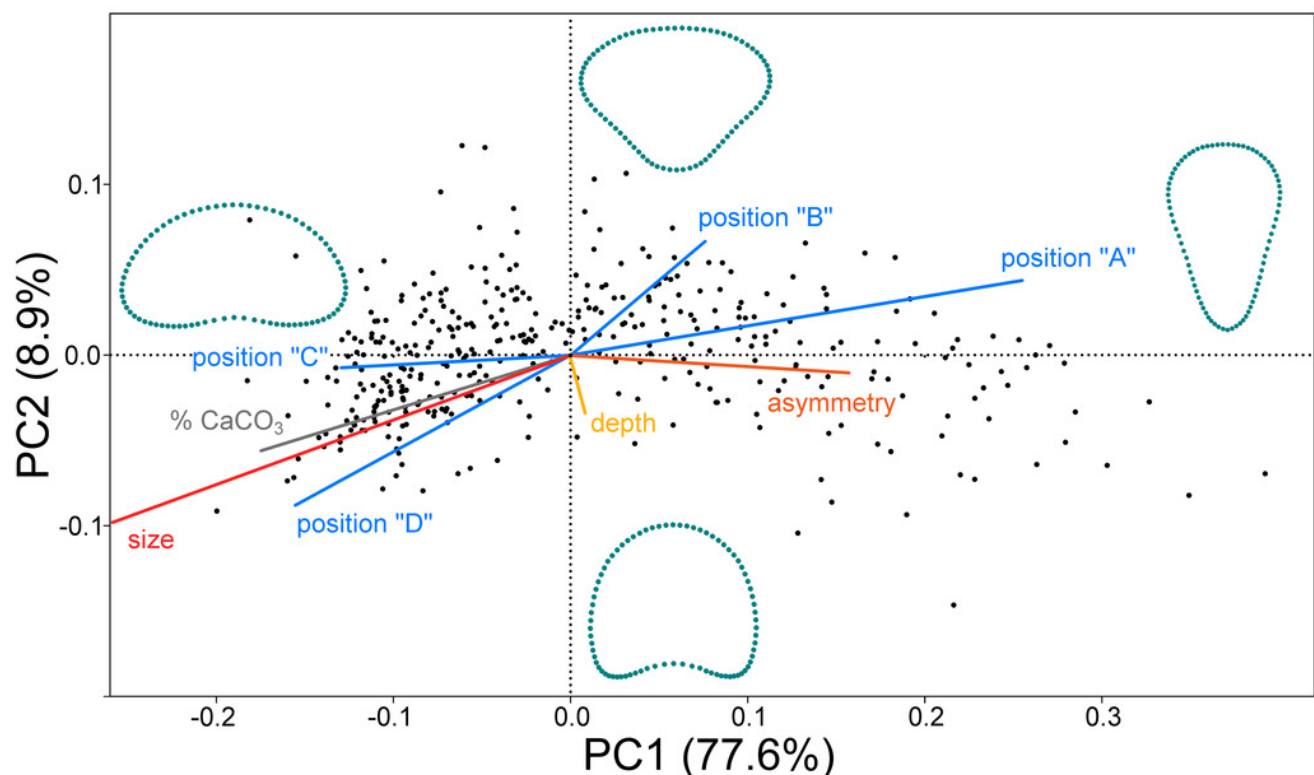
Figure 3

Patterns of shape change in segments of *Halimeda tuna* related to independent factors and their position on thalli.

The depicted shapes were reconstructed by a series of multivariate regressions of segment shape data on the six independent factors (size, CaCO3 content, thallus position A, B, C, D). Configurations depict segment shapes typical for marginal positions along the shape trajectories within the observed variability of the studied dataset.
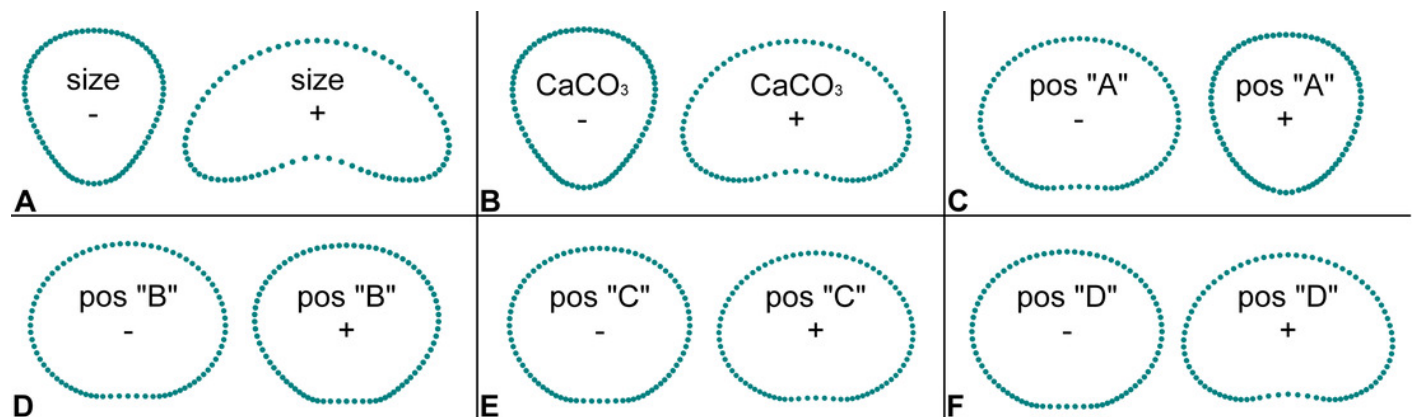
Figure 4

Correlation plot showing Spearman's non-parametric rank-order coefficients among tested independent factors.

The positive correlation is shown in blue, the negative correlation in red. Significant Bonferroni-corrected p-values lower than 0.0018 are marked by asterisks.
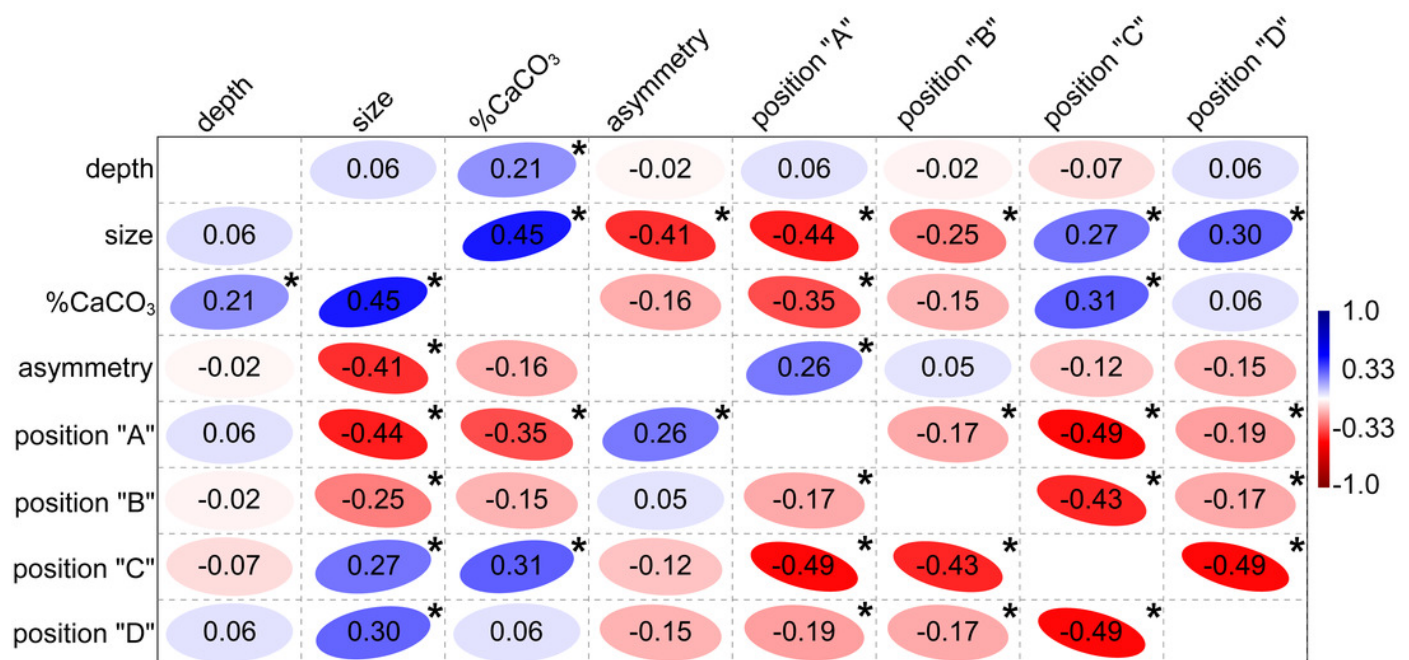
Figure 5

The linear correlation analysis of $CaCO_3$ content and segment size.

Pearson's r and the corresponding permutation p-value are depicted. Green curves indicate the 95% confidence intervals of the regression line. Colors correspond to positions of segments on branches as illustrated in Fig. 1B.
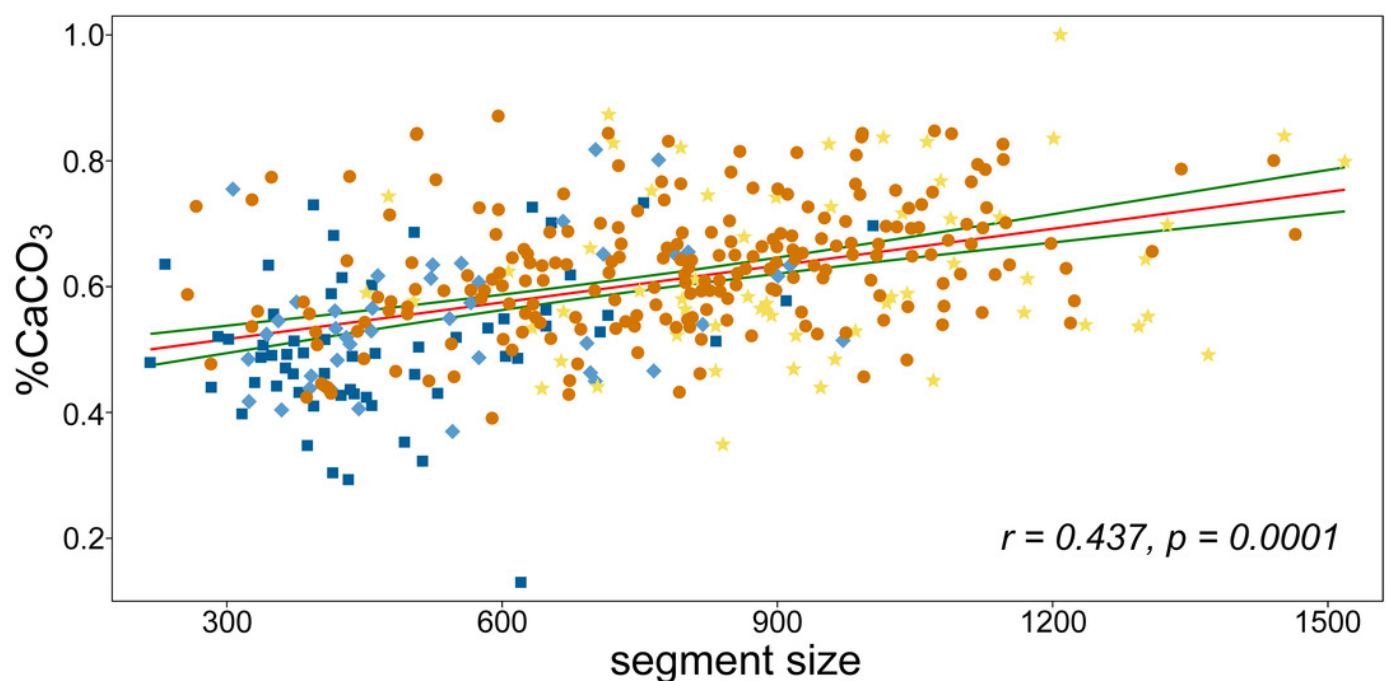
Results of linear correlation analyses between principal components yielded by PCA of shape data and external factors.

For each relationship Pearson's correlation and Spearman's non-parametric rank-order correlation coefficients are depicted. Significant Bonferroni-corrected p-values lower than 0.0016 are depicted in **bold**.

Table 1. Results of linear correlation analyses between principal components yielded by PCA of shape data and external factors. For each relationship Pearson's correlation and Spearman's non-parametric rank-order correlation coefficients are depicted. Significant Bonferroni-corrected p-values lower than 0.0016 are depicted in **bold**.

	eigenvalue	% variance	Pearson's *r* / Spearman rank-order linear correlation							
			depth	centroid size	% CaCO$_3$	asymmetry	position "A"	position "B"	position "C"	position "D"
PC1	0.01253	77.55	0.010 / -0.077	**-0.736 / -0.782**	**-0.368 / -0.379**	**0.330 / 0.329**	**0.523 / 0.468**	0.146 / **0.182**	**-0.259 / -0.216**	**-0.303 / -0.339**
PC2	0.00143	8.86	-0.086 / -0.116	**-0.282 / -0.285**	-0.126 / -0.117	-0.024 / 0.025	0.091 / 0.056	0.124 / 0.145	-0.020 / -0.003	**-0.176 / -0.185**
PC3	0.00089	5.48	-0.025 / -0.031	**-0.179** / -0.136	-0.048 / -0.006	0.098 / 0.094	0.071 / 0.053	-0.046 / -0.042	-0.032 / -0.044	0.015 / 0.046
PC4	0.00049	3.08	**-0.253 / -0.289**	-0.001 / -0.021	-0.029 / -0.035	0.015 / 0.014	-0.016 / -0.022	-0.085 / -0.062	0.104 / 0.112	-0.048 / -0.075

Results of permutational multivariate analyses of variance relating variation in segment shapes to different independent factors.

Significant Bonferroni-corrected p-values lower than 0.0063 are depicted in **bold**.

Table 2. Results of permutational multivariate analyses of variance relating variation in segment shapes to different independent factors. Significant Bonferroni-corrected p-values lower than 0.0063 are depicted in **bold**.

	$\sum PD_{ref}^2$	$\sum PD_{resid}^2$	$\sum PD_{pred}^2$	% explained	% unexplained	p
shape ~ depth	6.257	6.235	0.022	0.347	99.653	0.225
shape ~ centroid size	6.257	3.567	2.690	42.986	57.014	**0.001**
shape ~ %CaCO$_3$	6.257	5.583	0.674	10.773	89.227	**0.001**
shape ~ asymmetry	6.257	5.699	0.558	8.917	91.083	**0.001**
shape ~ position "A"	6.257	4.915	1.342	21.444	78.556	**0.001**
shape ~ position "B"	6.257	6.141	0.116	1.857	98.143	**0.006**
shape ~ position "C"	6.257	5.925	0.332	5.312	94.688	**0.001**
shape ~ position "D"	6.257	5.790	0.467	7.466	92.534	**0.001**

$\sum PD_{ref}^2$, sums of squared PDs between each specimen and the reference
$\sum PD_{resid}^2$, sums of squared PDs between each specimen and its predicted configuration
$\sum PD_{pred}^2$, sums of squared PDs of predicted fit
% explained, proportion of the total shape variation explained by the multivariate regression model
% unexplained, proportion of the residual shape variation
p, probability of the null hypothesis based on comparison of the original $\sum PD_{pred}^2$ with the distribution of the 999 random values yielded by the permutations of specimens among the values of the independent factors